Alexandria Engineering Journal 82 (2023) 1–15

Contents lists available at ScienceDirect

Alexandria Engineering Journal

journal homepage: www.elsevier.com/locate/aej

Original Article

Thermal efficiency of microchannel heat sink: Incorporating nano-enhanced phase change materials and porous foam gradient and artificial intelligence-based prediction

Somayeh Davoodabadi Farahani [a,*], Amirhossein Jazari mamoei [a], As'ad Alizadeh [b]

[a] School of Mechanical Engineering, Arak University of Technology, 38181-41167 Arak, Iran
[b] Department of Civil Engineering, College of Engineering, Cihan University-Erbil, Erbil, Iraq

ARTICLE INFO

Keywords:
Microchannel -heat sink
PCM
Spiral tube
Hybrid nanoparticles/PCM
Porous foam gradient
Artificial intelligence

ABSTRACT

This study investigates the impact of incorporating phase change materials (PCMs), nano-particles (NPs) enhanced PCMs (nePCMs), and porous foam gradients on the thermal performance (TPEF) of microchannel heat sinks (MCHS). Specifically, the effect of different PCM types, hybrid NPs, and spiral microchannels on the TPEF is examined using numerical solutions based on the finite volume method. The results indicate that increasing Re and using spiral microchannels significantly enhance the TPEF. The incorporation of NPs-water and PCM can reduce the thermal resistance (R) of MCHS, with PCM significantly improving the TPEF. Among the PCMs, ENCAPSUL demonstrates the best performance for MCHS. The combination of hybrid nePCM increases TPEF by approximately 9%. The combination of PCM-aluminum oxide-iron oxide NPs exhibits the highest TPFE. The use of a porous medium with PCM can decrease the R by about 60 %, and it improves the TPEF by altering the conduction and convection mechanism. various scenarios of changes in the porosity coefficient have been considered for porous foam gradient and the best performance is achieved for the NYPC mode. Various scenarios of MCHS with PCM-water combinations have been explored, and the best performance is observed when PCM is situated in the microchannel. Additionally, artificial intelligence techniques, such as the Group Method of Data Handling (GMDH), have been utilized to estimate R, and a multivariate polynomial regression (MPR) equation has been developed to calculate R based on input variables. GMDH is more accurate compared to MPR.

1. Introduction

A heat sink (HS) is a type of heat exchanger responsible for managing the heat generated in electronic or mechanical components. Its main function is to absorb the generated heat and distribute it to the surrounding fluid, usually air, to prevent an increase in temperature that could potentially damage the targeted part. The utilization of a HS becomes particularly important when using temperature-sensitive components in circuits or devices. By incorporating a HS, the undesired increase in temperature in these components is avoided. As a result, the lifespan of the parts is extended, as they operate within the acceptable temperature range stated in the data sheet. Additionally, the overall performance of the components and circuits is improved. Heat sinks can be categorized into two main types based on their operation: active and passive. With the introduction of micro-channel and mini-channel cooling systems, MCHS has become advantageous for cooling electronic devices and high-speed microprocessors [1]. These systems have high performance and a compact structure. Porous media and the nanofluid enhance the efficiency and heat transfer in the MCHS. Fluid flow in porous beds is also studied in the engineering disciplines. Farahani et al. [2] investigated the improvement of TPEF of a conventional MCHS using porous materials, PCM(Lauric acids), and Al2O3-H2O. They found that the TPEF of MCHS augments about 14–47%. Xiao et al. [3], Yan et al. [4] and Hasan and Muter [5] investigated the effect of different cooling fluids and the cooling TPEF of the MCHS. The TPEF of MCHS has been improved using an oscillating heat pipe, and a reported improvement of up to 21% has been achieved [6,7]. Shahsavar et al. [8] evaluated the TPEF of MCHS with water-Ag biological nanofluid. The findings show that the TPEF of MCHS increases with the strengthening of Re. Pourmehran et al. [9] scrutinized the efficacy of Cu&A1203-water on the TPEF of MCHS. The outcomes display that Cu-water is thermally more profitable compared to Al2O3-water. Haj Mohammadi et al. [10] presented the optimal design of porous medium-

* Corresponding author.
E-mail address: sdfarahani@arakut.ac.ir (S.D. Farahani).

https://doi.org/10.1016/j.aej.2023.09.054
Received 28 July 2023; Received in revised form 9 September 2023; Accepted 21 September 2023
Available online 29 September 2023

Nomenclatures

V	Velocity (m/s)
h	Convection heat transfer coefficient (W/m^2K)
t	Time (s)
A	Surface (m^2)
C_p	heat capacity (J/kgK)
D	Diameter (m)
Da	Darcy number
H	Height (m)
L	Length (m)
Nu	Nusselt number
P	Pressure (Pa)
Po	Poiseuille number
R	Thermal resistance (K/W)
Re	Reynolds number
W	Width (m)
k	Thermal conductivity (W/mK)
q	Heat flux (W/m^2)
N	The number of screws
x, y, z	Cartesian coordinate

Greek

K	Permeability coefficient (m^2)
β	Thermal expansion coefficient (K^{-1})
ε	Porosity coefficient
θ	Temperature (K)
Ω	Liquid fraction
μ	Viscosity $(Pa.s)$
ρ	Density (kg/m^3)
τ	Latent heat (J/kg)
φ	Volume fraction

subscripts

f	fluid
l	liquid
s	solid
w	wall
np	nanoparticles
nf	Nanofluid
hnf	Hybrid nanofluid
in	inlet

abbreviation

AI	Artificial intelligence
CDHT	Conduction heat transfer
CVHT	Convection heat transfer
FVM	Finite volume method
HS	Heat sink
HTC	Heat transfer coefficient
MCHS	Microchannel-heat sink
nePCM	Nanoparticles enhanced phase change material
NN	Neural network
NPS	nanoparticles
PCM	Phase change material
TPEF	Thermal Performance

MCHS to mend the TPEF of MCHS. They observed the TPEF of MCHS rises about 40%-90%. HajiMohammadi et al. [11] have reported that the application of a non-uniform magnetic field led to an improvement in MCHS TPEF of up to 10%. Other studies in the field of improving the TPEF of the MCHS with porous media were done by Ghorbani et al. [12], Li et al. [13] and Al Khasawneh et al. [14]. They stated that the porous medium has a positive influence on the TPEF of the MCHS. Also, Chu et al. [15] found that the AIN-Al_20_3-water enhances the TPEF of MCHS. Ho et al. [16] assessed the TPEF of the MCHS with nanofluid experimentally and showed that the maximum amount of reduction in thermal resistance obtained by using water-Fe3O4 is 12.61%. The effect of the MCHS composition of porous rectangular bars on the TPEF of the MCHS has been investigated by Li et al. [17]. The outcomes show that these changes enhance the TPEF of the MCHS. The effects of using rectangular fins [18], ferrofluid [19], different nanofluids [20] and hybrid nanofluids [21] on the performance of MCHS have been investigated and all these studies have reported improved performance of MCHS. Bazkhane and Zahmatkesh [22] simulated and discussed the TPEF of MCHS with alumina-water nanofluid and porous medium. They reported that the major contribution in reducing the overall TPEF is related to the porous substrate. Another factor influencing the TPEF of the MCHS is the geometrical shape of the microchannel. Rajabifar [23] evaluated the TPEF of a 3D two-layer MCHS. The outcomes disclosed that by using the planned arrangements, TPEF is increased and the difficulties associated with progressive cooling are significantly eliminated. In a study [24], the effect of parallel and opposite flow in a double-layer microchannel with a branch on the TPEF of the system was discussed. Hatami et al. [25] scrutinized the TPEF of a fin-shaped MCHS with water-Cu. Accordingly, the temperature alteration between the coolant and the wall lessens. Tang et al. [16] investigated the efficacy of reducing the cross-sectional area along the microchannel on the TPEF of the MCHS. Maheswari et al. [26] did a 3D numerical examination to augment the TPEF of MCHS performance by the double-layer(DL) microchannel. The TPEF of DL MCHS is more than the normal design. Srivastava et al. [27] explored the effect of using single-layer and double-layer rectangular microchannels with and without branching plates on the TPEF. The results display that the TPEF rises by around 40% for the two-layer microchannel. Jing et al. [28] inspected the influence of different cross-sections on the TPEF of MCHS. The results show that the TPEF of MCHS decreases with the increment in the hydraulic diameter of the microchannel. The use of phase change materials (PCMs) [29–31] in short-term phase change graphs provides an effective way to regulate temperature fluctuations and maintain a consistent and safe thermal environment [32–36]. PCMs have various applications in energy storage devices [37–39], and researchers have made significant efforts to improve the thermal properties of these materials in order to increase their thermal conductivity [40]. Ramesh et al. [41] numerically analyzed the increase in the TPEF by incorporating paraffin-PCM. They reported that R is about 7.3% lower compared to MCHS without PCM. Dai et al. [42] investigated the TPEF of graded porous, and microencapsulated PCM(MPCM) suspension on the TPEF of the MCHS. They showed that the TPEF augments about 61%. Dai et al. [43] surveyed the consequence of PCM microcapsules and porous medium on the TPEF of the MCHS. The simulation results show that R is lower by increasing the speed of water-microcapsules of PCM compared to the base state. Wang et al. [44] discovered the TPEF of MCHS with Co2/R32 condensation and the porous medium. Vajdi et al. [45] evaluated the PEF of a MCHS made of ZrB2 ceramic numerically. They stated that the significant thermal conductivity of ZrB2 results in high heat dissipation and high heat transfer rates.

Based on the studies, there is a lack of knowledge in the area of thermal behavior and performance of MCHS integrated with nePCM and porous gradient foam, as limited quantitative studies have been conducted on this topic. In this examination, the efficacy of PCM, porous medium and single and hybrid nanoparticles on the TPEF of MCHS has been investigated. The working fluid in the microchannel is water and$Re < 1000$. The impact of different types of PCM, each with unique thermal characteristics, and the influence of combining single and

hybrid nanoparticles with PCM on the TPEF of MCHS have been discussed. Furthermore, the effect of various porous medium properties, such as porosity coefficient (ranging from 0.4 to 0.99), Darcy number (ranging from 0.0001 to 1), and the type of porous medium (steel, aluminum, copper, and silicon carbide), on the TPEF has been examined. Also, the influence of using a porous foam gradient, in which the porosity coefficient changes linearly in different directions, has been evaluated on the TPEF of the desired system. The numerical solution is based on the finite volume method. and the TPEF has been estimated using advanced calculations, including the Group Method of Data Handling (GMDH) and multivariate polynomial regression (MPR).

2. Explanation of the problem

A graphic of the MCHS with six microchannels with a considered circular cross-section is revealed in Fig. 1. The fluid in the MCHS is water. The dimensions of the block are $12 \times 12 \times 2$ mm^3 and the diameter of the microchannel is 0.7 mm. To explore the efficacy of microchannel changes along the flow, considering the straight mode (C0) and spiral mode(C1) as shown in Fig. 1 and changing the pitch between the spirals (N) are discussed. The efficacy of PCM, porous medium and nanoparticles-PCM under the active surface on the TPEF of the MCHS has been investigated. $q = 300$ W /cm^2 is employed on the top plate of the MCHS as revealed in Fig. 1. The flow in the microchannel is laminar and $50 < Re < 800Re$. The inlet temperature of the flow to the microchannel is 300 K. $V = 0$ is applied to all walls in contact with the fluid. The boundary condition of symmetry is considered on the left wall according to Fig. 1, and the rest of the walls exposed to the MCHS, containing the upper and side walls, are thermally insulated.

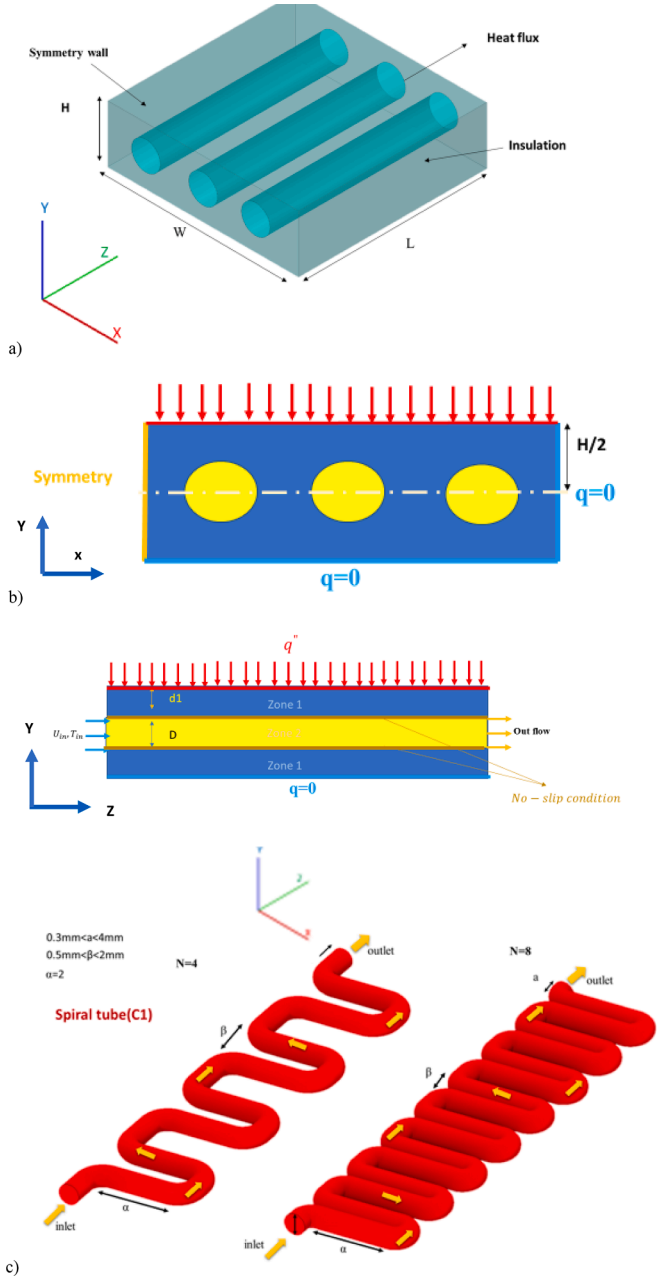

Fig. 1. a) A graphic of the problem, b) boundary condition, and c) various states of spiral mode.

The fundamental equations that govern the problem are provided as follows [35,46]:

$$\varepsilon \frac{\partial \rho_f}{\partial t} + \nabla . \left(\rho_f \vec{V} \right) = 0 \tag{1}$$

$$\rho_f \left(\frac{\partial \vec{V}}{\partial t} + \vec{V} . \nabla \vec{V} \right) = -\vec{\nabla} P + \nabla (\mu_f \nabla \vec{V}) + Au \frac{(1-\lambda)^2}{(\lambda^3 + 0.001)} \vec{V} + \rho \beta \varepsilon \vec{g} (\theta - \theta_l) - \left(\frac{\mu_f}{K} + \frac{1.75 \rho_f}{\sqrt{150 \varepsilon^5 k}} \left| \vec{V} \right| \right) \vec{V} \tag{2}$$

$$\rho_f (C_{p,f} + \tau \frac{d\Omega}{d\theta}) \frac{d\theta}{dt} + \rho_f C_{p,f} \vec{V} . \nabla \theta = (\varepsilon k_f + (1-\varepsilon) k_s) \nabla^2 \theta \tag{3}$$

where $V, \varepsilon, \rho, \mu, C_p, P, K, \beta, t, g, \tau, \theta$ and k represent velocity, porosity coefficient, density, dynamic viscosity, heat capacity, pressure, the permeability of porous material, thermal expansion coefficient, time, gravity acceleration, latent heat, temperature and the thermal conductivity coefficient, respectively. s & f are solid and fluid. Au is the paste region constant and is equal to 10^5, and Ω is the liquid fraction. Darcy and Reynolds numbers are expressed as follows [2,36,47]:

$$\mathrm{Da} = \frac{K}{L^2} and Re = \frac{\rho U_{in} D}{\mu} \tag{4}$$

where L & D are the length and diameter of the microchannel, respectively, Also, the heat equation in the solid environment is included as follows:

$$k_s \nabla^2 \theta_s = 0 \tag{5}$$

When nanofluid flow is used in the MCHS, the fluid properties change and relationships can be used to calculate nanofluid and hybrid nanofluid properties and the desired relationships are given in Fig. 2. φ is the volume fraction of NPS and$n = 3$. The f, nf, np, and hnf indices represent fluid, nanofluid, nanoparticles, and hybrid nanofluid, respectively. 1 and 2 represent the first and second NPS, respectively. Po number, Nusselt number (Nu), thermal resistance is defined below:

$$Po = \frac{1}{2} \frac{\Delta P}{\rho_f U_{in}} \frac{\mathrm{D}}{\mathrm{L}} \times Re \tag{6}$$

$$Nu = \frac{-D \frac{\partial \theta}{\partial x channelwall}}{\theta_w - \theta_{in}} \tag{7}$$

$$R = \frac{\theta_{w,max} - \theta_{f,in}}{qA} \tag{8}$$

The porous foam material, NPS and PCM is considered to be (Al, Cu, steel (AISI316), Sic), (Ag, Fe3O4, Al2O3, SiO2, Cu, MgO and MWCNT) and (C21, C24, CCH, RT35, RT50, RT82, RT42, RT27, RT58, RT21, RT25 & ECAPSUL). The features of all the materials are given in Table 1. In this study, the θ and V fields were simulated using ANSYS FLUENT software. The coupling of the P and V fields was achieved using the SIMPLE method based on the FVM. The diffusion and convection terms were discretized using the second-order Upwind method and the central

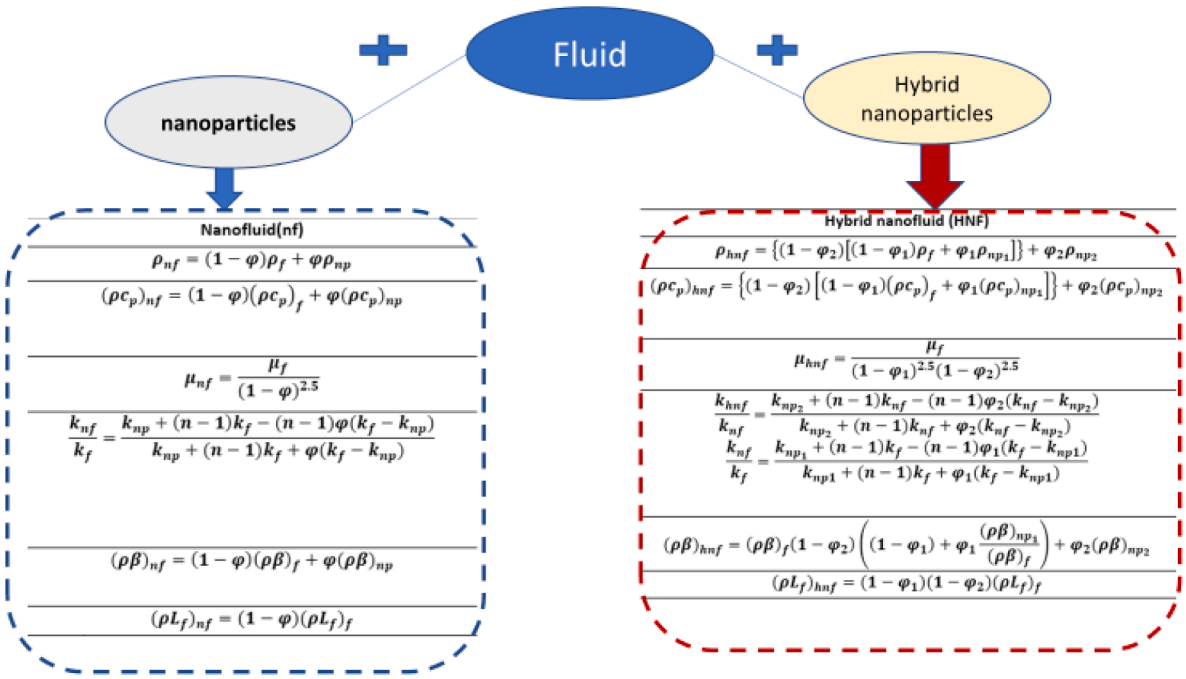

Fig. 2. The correlation for computing the properties of NF.

Table 1
Thermal properties of the materials.

Property	θ(S/l) [K]	C_p [J.kg^{-1}K^{-1}]	τ [J.kg^{-1}]	ρ [kg.m^{-3}]	k [W.m^{-1}.K^{-1}]	β [K^{-1}]	μ [Pa.s]
Ag[48]	–	235	–	10,500	429	0.000026	–
Al[49]	–	0.87	–	2719	202.4	–	–
Al2O3[50]	–	765	–	3970	46	0.0000085	–
Calcium chloride hexa hydrate (CCH)[51]	223.14–303.15	2060	170,000	1710	1.09	0.0005	0.01
Climsel c21[52]	294.15–299.15	3600	144,000	1380	0.7	0.0005	0.01
Climsel c24[53]	297.15–300.15	3600	151,300	1380	0.7	0.0005	0.01
Cu[48]	–	385	–	8933	401	0.000016	–
encapsulated sp-25 A8[54]	288.15–303.15	2500	180,000	1380	0.6	0.00091	0.00342
Fe_3O_4[50]	–	670	–	5200	6	0.0000118	–
MgO[50]	–	955	–	3560	45	0.0000126	–
MWCNT	–	730	–	2640	15	0.00007	–
RT21[55]	291.15–296.15	2100	34,000	893	0.21	0.0005	0.00342
RT25[55]	295.15–299.15	2000	148,000	800	0.2	0.0006	0.026
RT27[55]	300–302.15	2000	189,000	880	0.2	0.0005	0.02
RT35[55]	302–308	2100	157,000	820	0.2	0.00092	0.0027
RT42[55]	311.15–315.15	2000	165,000	760	0.2	0.0005	0.02351
RT50[55]	318–324	2000	168,000	780	0.2	0.00091	0.006
RT58[55]	321–335	2100	180,000	840	0.2	0.00011	0.0269
RT82[55]	351.15–355.15	2000	176,000	860	0.2	0.001	0.03499
SiC[56]	–	750	–	3000	120	0.0004	–
SiO_2[48]	–	745	–	2220	1.38	5.5E-07	–
Steel[49]	–	441	–	7882	35	0.0001	–
water[49]	273.15–373.15	4182	340,000	997	0.6	0.000295	0.001003

finite difference method, respectively. Convergence was determined by reducing the sum of absolute values of relative errors by five orders of magnitude. To guarantee the independence of the results from the grid geometry, different grids with varying dimensions (coarse and fine) were selected, with the heat flux surface temperature serving as the benchmark parameter.

Fig. 3 shows the temperature distribution along the channel using four different grid sizes: M1(60016), M2(107786), M3(435060), and M4 (2750490). In this section, $Re = 50$, and water is used as the fluid. As the grid size decreases, the results converge to a certain value. Based on these results, it can be concluded that for the M3 grid, the results are not affected by the grid size, and there is only a small difference (less than 0.01%) between the results of the M3 and M4 grids. Therefore, the M3 grid was chosen as the final grid. Fig. 3 provides an overview and a close-up view of the computational grids used in the problem's geometry. To confirm the accuracy of the simulation results, a comparison was made with the experimental work directed by Phillips et al. [57] and revealed in Fig. 3. The relative difference between the two sets of results is less than 2.7%, indicating the precision of the proposed modeling approach.

3. Explanation of results

3.1. Efficacy of geometrical parameters and adding NPS

Thermal resistance (R) measures a material or system's ability to resist heat flow. Evaluating MCHS based on R provides quantitative data on heat dissipation. Comparing different designs or materials' R helps assess their efficiency in cooling. Lower R indicates a more effective

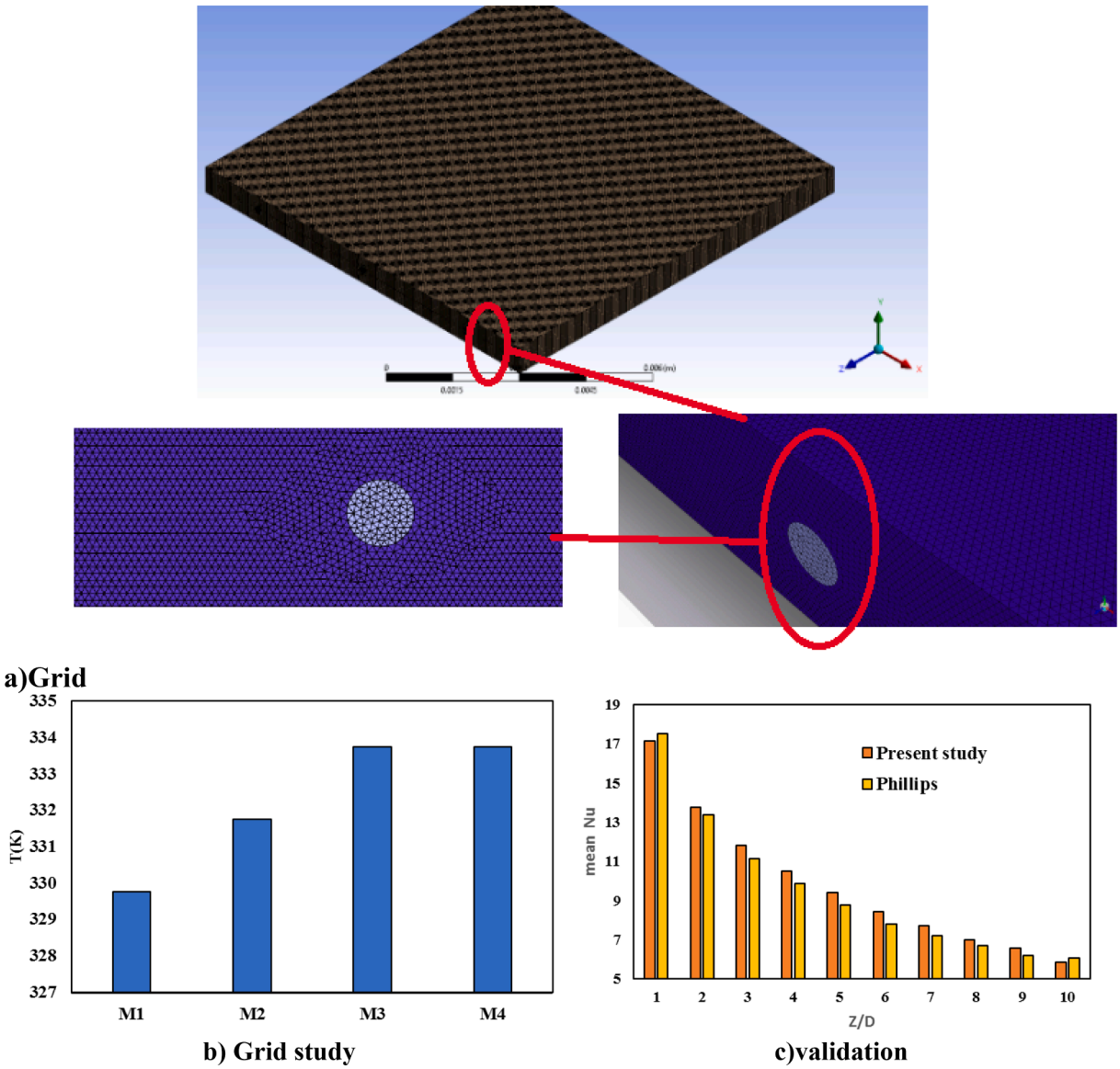

Fig. 3. A) A view of the grid) grid study, and c) validation of the current results with ref. [57].

cooling system, preventing device overheating. Nonetheless, R is a useful indicator in evaluating MCHS. Fig. 4 shows the efficacy of geometrical parameters on the R. With the intensification in Re, there is a reduction in R in both smooth (C0) and spiral pipes(C1). As Re rises, the flow rate also increases, resulting in enhanced convection HTC in the channel. This allows more heat to be absorbed, leading to cooling of the active wall and a reduction in θ_w. When the tube takes the form of a spiral (C1), the swirling flow generated by the spiral shape improves CVHT and further decreases the wall temperature compared to the C0 state. Consequently, the R is lower in the C1 compared to the C0. The R in the spiral mode(C1) is lower than the straight mode(C0) by approximately 80% and 38% for$Re = 50$ and 800, respectively. In the case of C0 and C1, R decreases by 74% and 61% as Re changes from 50 to 800. The impact of tube diameter on the ratio of R in the C0 has been examined. Increasing the diameter from 0.22 to 0.65 results in a decrease of approximately 74% in R. Furthermore, increasing the distance from the active surface ($d1$) leads to an increase in R, with a 0.8% increase observed when the $d1$ increases from 0.25 to 0.75 mm. Because the heat conduction resistance rises with the distance from the active surface and the ability to dissipate heat by the microchannel. In the C1, increasing N (in the C1 state) results in a decrease in R, as convection HTC is enhanced. Increasing N from 1 to 8 leads to a decrease of approximately 10.5% in R. The effect of adding NPS to the working fluid on R is shown in Fig. 4. It is assumed that the nanofluid is completely stable and no sedimentation occurs. The presence of NPS and an increase in φ improve the PEF of MCHS compared to the state with$\varphi = 0$. Additionally, Al2O3-NPS shows less improvement compared to Fe3O4-NPS.

This issue pertains to the properties of NPS and their thermal capacity, namely how much they can enhance thermal diffusion in the microchannel. These NPS provide higher k, diffusivity, and increased surface area, leading to improved heat transfer rates. The increase in heat dispersion in the microchannel leads to a rise in the average fluid temperature, which enhances the convection HTC and boosts the convection in the MCHS, resulting in a reduction in R compared to the state without nanofluids. Consequently, the addition of NPS and an increase in nanofluid concentration enhance the HTC in all cases. Additionally, the effect of increasing φ becomes more pronounced as HTC increases. For iron oxide and aluminum oxide nanoparticles, the decrease in R is 8.6% and 4.3% for the C0 and 8.3% and 5.1% for the C1, respectively, when φ increases from 0.01 to 0.05.

Fig. 5 illustrates the temperature variations in terms of Re for the C0&C1 states. The results indicate that θ_w declines as Re rises. When Re

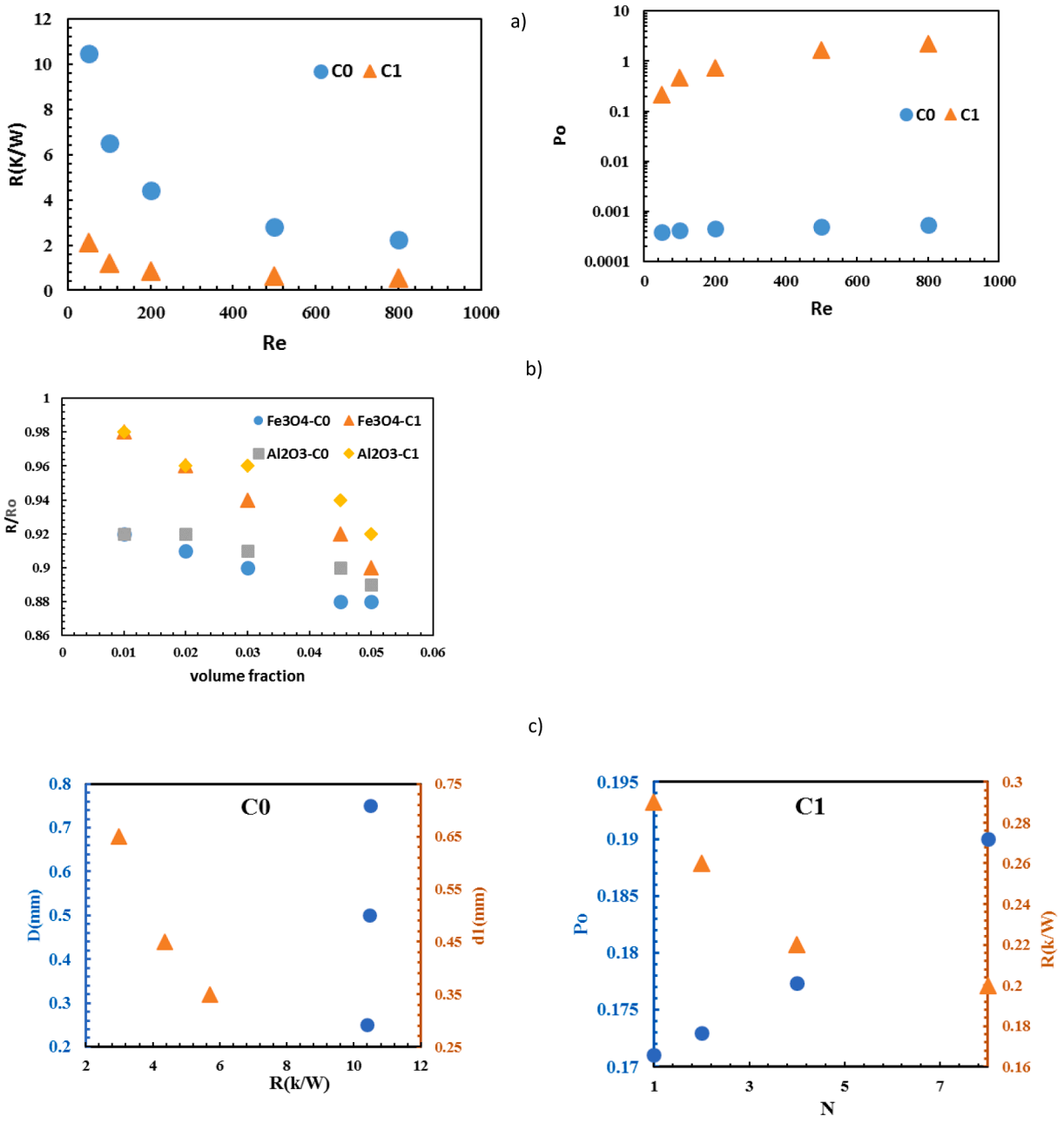

Fig. 4. The effect of a) Re, and b)φ, and c) the geometrical parameter on the TPEF in the Co and C1 cases.

is altered from 50 to 800, θ_w decreases by 7.4% and 1.5% for the C0&C1, respectively. As *Re* intensifies due to higher flow rates, the fluid temperature within the microchannel changes less. In the case of MCHS, the temperature is lower with the C1 compared to the C0. The temperature in the C1 is approximately 7.31% and 1.5% lower than in the C0 when *Re* is changed from 50 to 800. This is due to the spiral mode(C1) generating secondary flow and enhancing mixing, resulting in improved heat dissipation. Additionally, the surface area of the microchannel in contact with the aluminum block is greater in this scenario.

3.2. Efficacy of PCM and nePCM

The influence of using various types of PCM on the TPEF of MCHS is illustrated in Fig. 6. R series PCMs and CCH increase the θ_w and reduce the TPEF. Utilization of C21, C24, and ECAPSUL promotes heat dissipation from the active surface, resulting in a reduction in θ_w and an improvement in the TPEF. Among the PCMs, PCM-ENCAPSUL exhibits the lowest *R*, while RT82 demonstrates the highest *R* compared to the scenario without PCM. This discrepancy can be attributed to the varying latent heat and melting temperature of each PCM. Generally, PCMs with higher latent heat exhibit lower *R*. The distinction in the thermal characteristics of the PCMs under identical conditions is explicitly evident in their melting fraction history, as depicted in Fig. 6. For instance, RT21 melted completely and rapidly, whereas CCH only melted about 0.41 of it within 1000 s. The *R* values for PCMs such as CCH, RT25, RT21, RT58, RT27, RT42, RT82, RT50, and RT35 increased by 38%, 96%, 177%, 81%, 11%, 82%, 73%, and 30% respectively. On the other hand, the *R* values for C24, C21, and ECAPSUL PCMs decreased by 42%, 54%, and 62% respectively. RT21 demonstrated the best performance in terms of reducing melting time among different PCMs, with complete melting achieved in 200 to 400 s compared to other PCMs. With the increase of *Re*, the *R* values for C21 decreased by 45.27%, 46.08%, 46.80%, 47.48%, and 47.70% atRe = 800, 500, 200, 100, and 50 respectively, compared to the state without PCM. Additionally, the melting fraction

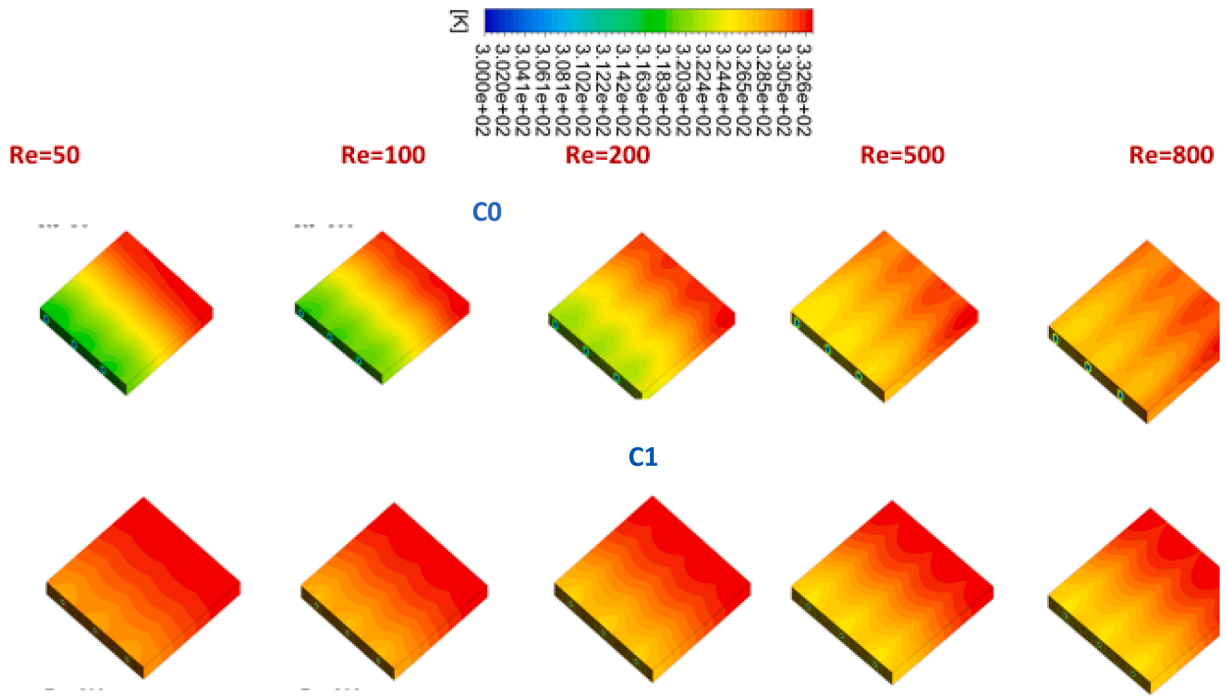

Fig. 5. Temperature contours of MCHS with Re with N = 8.

decreased with the increase of Re. For example, at$Re = 800$, compared to$Re = 50$, Ω has decreased by about 1.7%. C21 is considered as PCM for further investigations. The effect of rising the *Re* on the TPEF of MCHS-PCM and the average melting fraction has been investigated. With the increase of Re, R and the average melting fraction has increased. PCM has a low conductivity coefficient and with the increment of *Re*, the flow speed inside the microchannel increases and the speed of heat transfer from PCM to the fluid inside the microchannels decreases. Therefore, the heat obtained from the active surface is used to melt more PCM and less heat reaches the fluid inside the microchannels. The increase in melting of PCM under the active surface and the low conductivity coefficient of PCM make happen to an intensification in the θ_w and an increment in *R*. Therefore, at$Re = 50$, a better performance than MCHS has been observed. The history of melting fraction shows insignificant changes in melting fraction with *Re*. Of course, it should be considered that the use of PCM helps to save thermal energy. Fig. 6 shows the contour of temperature changes for$Re = 50$, 200 & 800 in terms of time. When PCM is used, due to its high heat absorption ability, it absorbs a large part of the generated heat in the active surface and reduces θ_w. In the beginning, this ability is more, and with the passage of time, this ability lessens and the θ_w rises. With the increase of *Re*, the flow speed inside the microchannel increases and the heat transfer rate from PCM to the fluid inside the microchannels decreases. Therefore, a higher temperature is observed on the active surface with an increase in *Re*.

Fig. 7 illustrates the impact of mono and hybrid NPS-PCM on the TPEF and liquid fraction. The NPS concentration (φ) is maintained at 1–2%. It is observed that at Re = 50 and φ = 2%, the *R* experiences the greatest decrease. PCM has a low *k*, resulting in slower heat transfer. However, the addition of NPS improves the *k*, enhancing heat dissipation and reducing θ_w. Consequently, the TPEF improves. Changing in *R* for PCM with MWCNT, Cu, Ag, Fe3O4, SiO2, A12O3, MgO NPS at $\varphi =$ 0.01&0.02 for$Re = 50$ is about (1.08,1.97%, 1.8%, 3.1%, 0.59%, 2.09% and 1.68%) and (1.52%, 2.3%, 3.6%, 1.23%, 2.39%,2.61%, 1.6%) respectively, compared to the $\varphi = 0$. As a result, Fe3O4has the best *R* among nanoparticles with $\varphi = 0.02$. Also, the effect of hybrid NPS (HNPS) of MgO-Ag, A12O3-Cu, SiO2-MWCNT, A12O3-Fe3O4 on the *R* has been investigated. The base case is MCHS-PCM without nanoparticles. The φ is considered to be 2%. With the rise of *Re*, the *R* decreases in the case of PCM-HNPS. By adding HNPS, the conductivity coefficient of PCM and the ability to transfer heat through molecular diffusion increases, which leads to the rapid melting of PCM. In this case, the *R* for A12O3-Fe3O4, SiO2-MWCNT, A12O3-Cu, MgO-Ag in $\varphi =$ 0.02% for$Re = 50$ decreases about 3.9%,0.76%,6.31, 5.95%, compared to the $\varphi = 0$, respectively. Also, adding NPS to PCM reduces the conduction resistance. As a result, Al2O3-Cu has the best *R* among nanoparticles with $\varphi = 0.02$. The efficacy of *R* and liquid fraction with *Re* for Al2O3-Cu-PCM has been examined. Increasing *Re*, which reduces the convection resistance in the heat transfer path and increases the ability of the mentioned system to remove heat from the active surface and improve the TPEF. It has been observed with an increase of$Re = 50$ to 800, about a 67.1% decrease in *R*. The lower the ability to dissipate heat, this energy will only melt more of the PCM composition.

3.3. *Efficacy of porous foam gradient*

The effect of using foam gradients beneath the active surface (zone1) on the TPEF of MCHS is depicted in Fig. 8. In a natural porous environment, the shape and size of pores are irregularly distributed. As a result, the heat transfer and thermal performance enhancement factor (TPEF) of MCHS can be influenced by the permeability,ε and matrix material. A porous medium is used in the zone1 where the PCM is located. First, the effect of *Da* on the TPEF has been investigated in Fig. 8. The *Da* is considered within the range of 0.0001 to 1. The presence of the porous medium improves the TPEF in heat dissipation. The porous medium elevates the conductivity coefficient of PCM, thereby improving the conductive heat transfer in this section and enhancing the heat transfer capability to the microchannel. When the penetration of the fluid in the porous medium increases, it does not have a significant effect on the *R*. Of course, the improvement of conductive heat transfer in the PCM region improves the melting process and increases the average melting fraction compared to the state without porous medium. The efficacy of ε on *R* and the average melting fraction at$Re = 50$, & Da=0.001 has been investigated in Fig. 8. It is observed that increasing ε from 0.4 to 0.99 leads to an increase in *R*, with this change being more prominent after $\varepsilon = 0.9$. The melting fraction decreases as ε increases because, initially, CDHT is effective during PCM melting. However, as

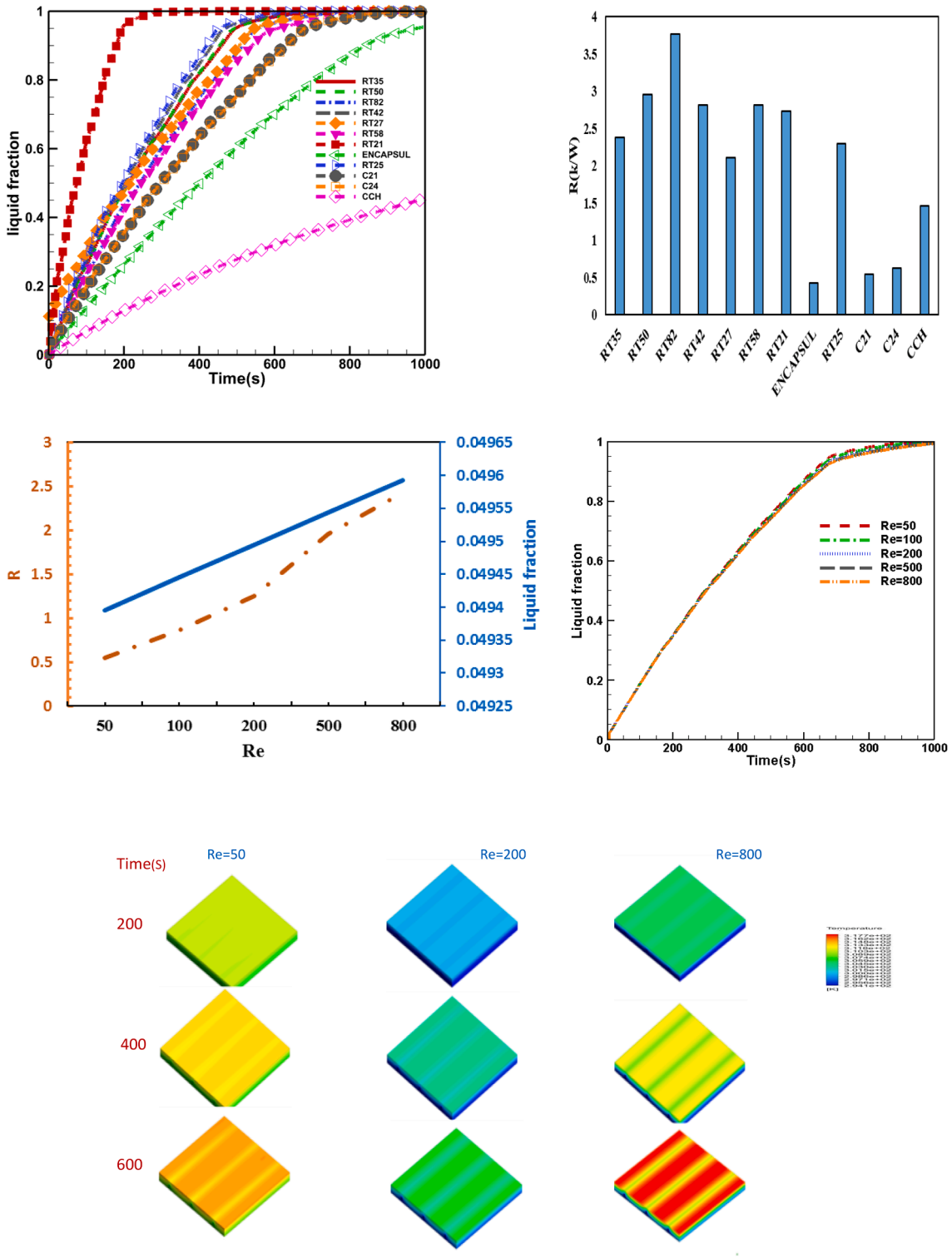

Fig. 6. Efficacy of a) various types of PCMs, b) various Re on the TPEF and liquid faction and temperature contours.

the PCM melts and a heat transfer in the liquid layer forms, natural convection becomes dominant, resulting in increased convection resistance with higher ε values. Consequently, the average melting fraction decreases with an increase in ε, although this decrease is less than 1%. The effect of the type of matrix of the porous medium on the TPEF of MCHS and the average melting fraction has been investigated. The material of the matrix is Steel, Al, Cu and Sic. The results indicate that steel and copper have the highest and lowest R, respectively. Among the investigated materials, Cu has a higher thermal conductivity coefficient and its combination with PCM increases the effective thermal conductivity coefficient. Finally, the conductive resistance in the direction of heat transfer decreases and in this case more heat is removed from the active surface and *R* decreases. Of course, the removal of heat from the PCM environment leads to a decrease in the melting rate. After Cu, first Al and then Sic have the lowest *R*. In this case, *R* for Sic, steel, and Cu has changed by about 30.35% ,1.67%, and −3.31% compared to Al, respectively. The average melting fraction for Sic, steel and Cu has changed about 0.7%, 0.003%, and −0.34% compared to Al.

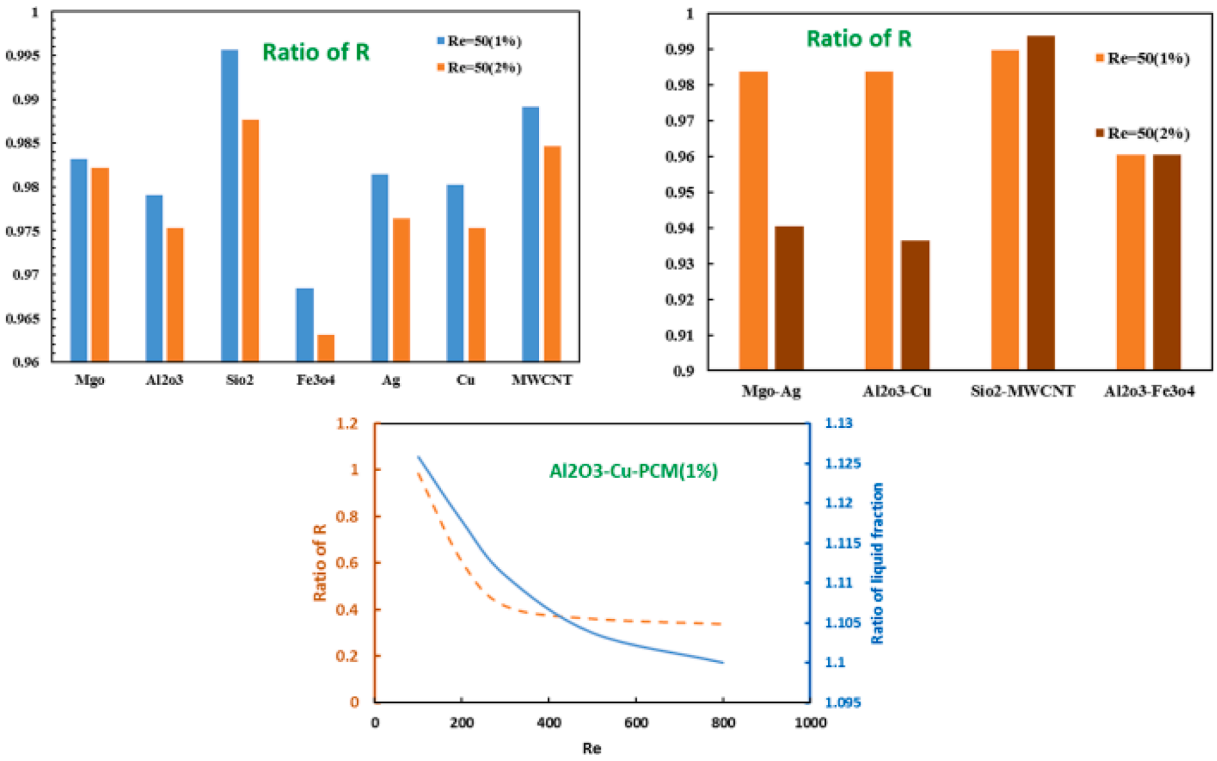

Fig. 7. The effect of nps-pcm on mchs performance and liquid fraction.

Additionally, another scenario was considered where ε increased or decreased along one of the coordinate axes for further investigation. Six cases have been considered and the effect of linearly changing ε on the TPEF and the average melting fraction has been discussed. It can be observed that NYPC has the lowest R, while NZPC has the highest *R*. In comparison to the case of uniform ε, *R* has improved in the six mentioned cases. The porosity gradient in PYPC and NYPC is in the direction of heat transfer. In the case of PYPC, near the active surface, ε is higher, leading to increased convection resistance and decreased conduction resistance. This initially promotes heat absorption and melting of PCM. However, as the molten PCM layer grows over time, the natural CVHT mechanism is activated, and the increase in ε negatively affects this mechanism, resulting in a decline in the heat transfer rate. and increased convection resistance, facilitating faster heat dissipation through molecular diffusion. Consequently, *R* is lower in NYPC compared to PYPC. Both natural convection and thermal conduction mechanisms play a role in heat dissipation. Towards the final stages of PCM melting, the reduction in convection resistance and the increase in thermal conduction can be highly effective in increasing the average melting rate. In fact, the average melting fraction in NYPC is approximately 0.06% higher than PYPC. In NYPC, ε increases as one moves away from the active surface. This leads to lower conductive resistance. The direction of porosity gradient in NXPC and PXPC is perpendicular to the main direction of heat transfer. The changes in the porosity coefficient are linear along the active surface. For PXPC, on the left side of the geometry, the conduction resistance and convection transfer are at their lowest state, and the conduction resistance and natural convection increase as you move along the x-axis.

For NXPC, on the left side of the geometry, conductive resistance and convection transfer are at their maximum, and as you move along the x-axis, conductive resistance and natural convection decrease. Anyway, the distribution of two mechanisms of convection and conduction in the PCM environment is very effective in absorbing heat from the active surface. The difference in *R* for NXPC and PXPC modes is less than 0.06%, and NXPC mode performed slightly better. The mode of NZPC and PZPC is the same as the previous mode, but with the difference that, in addition to the cases of the previous mode, the ε changes along the movement of the flow inside the microchannel. In the case of PZPC, in the flow direction, the conductive resistance and natural convection increase in the PCM-porous medium. In the case of NZPC, in the opposite direction of the flow in the microchannel, the conductive resistance and natural convection increase. At the beginning of the microchannel, the convection resistance is low for the flow inside it, and as the fluid flow progresses along the channel, the convection resistance increases. Therefore, the result of these changes can help to remove more heat from the active surface, and in the case of NZPC, the thermal resistance is about 2% lower than that of PZPC. The average melting fraction for the six cases differs by less than 0.01%. The changes in the melting fraction for different states of the porous foam gradient are shown in Fig. 9. In any scenario, when the ε is lower, the conduction resistance decreases, resulting in a higher melting fraction due to increased heat absorption by the PCM from the active surface. As time passes, the heat transfer mechanism in the PCM transitions to convection. In areas with higher ε, CVHT becomes dominant, aiding in melting more PCM and removing heat from the active surface. The NYPC & NZPC modes exhibit the lowest temperatures compared to other modes. The placement position of PCM has been evaluated by considering four modes in the microchannel as illustrated in Fig. 10. The first case (state1) involves using two tubes, where the inner radius is half that of the outer radius of the microchannel. The results demonstrate that the presence of PCM in the microchannel enhances the TPEF of MCHS and significantly reduces the R compared to the case without PCM. Among the considered modes, state3, where the PCM is located inside the microchannel, exhibits the best TPEF and lowest θ_w. When the PCM is inside the microchannel, the high thermal conductivity coefficient of aluminum facilitates heat transfer from the active surface to the PCM, causing the PCM to melt by absorbing this heat. This combination results in a lower θ_w compared to other states, as revealed by the temperature contours showing a uniform distribution for state 3 compared to other states.

Furthermore, it was observed that the state with the highest average melting fraction was state 2, while the state with the lowest average melting fraction was state 3. In this scenario, the *R* of state 1 and state 3

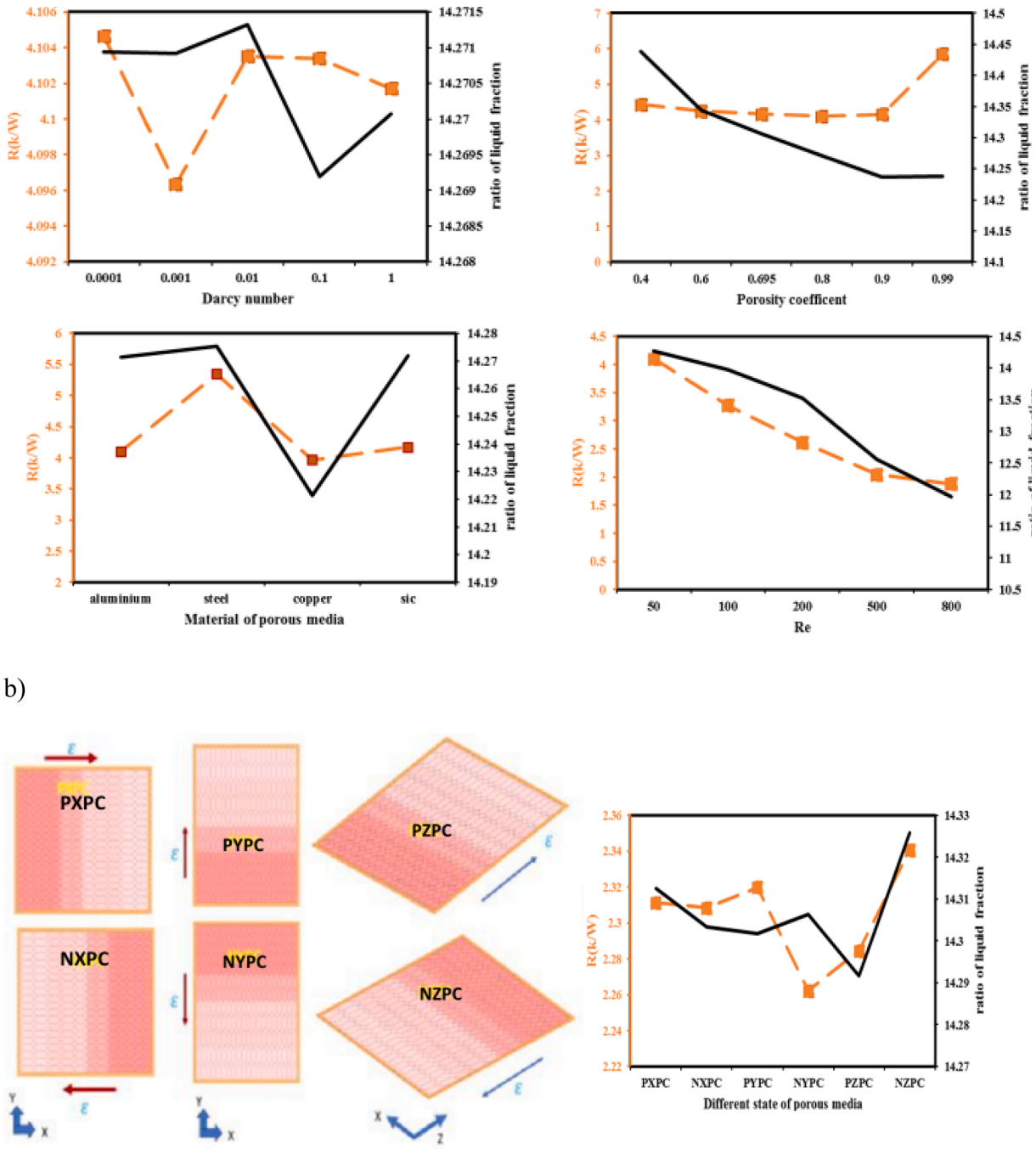

Fig. 8. The effect of a) features of porous media and b) porous foam gradient on the PEF and liquid faction for C0 with PCM.

increased by 6.66% and 35.24%, respectively, compared to state 4. On the other hand, state 2 experienced a decrease in *R* of 28.07% when compared to state 4. Regarding the average melting fraction, state 1 and state 3 showed an increase of 28.67% and 241.25%, respectively, in comparison to state 4. Meanwhile, state 2 exhibited a decrease of 10.68% compared to state 4.

The findings of the current study on enhancing the thermal efficiency of MCHS through the utilization of porous gradient foam and PCM (or nePCM) offer valuable knowledge for the development and optimization of electronic devices. This technology enables manufacturers to improve the effectiveness and durability of electronic devices, ultimately benefiting the end users.

3.4. Prediction of the TPEF of MCHS

As mentioned in the previous sections, the current research focuses on evaluating MCHS based on thermal resistance. In this section, an estimation of thermal resistance has been conducted using soft calculations based on artificial intelligence.

3.4.1. Group method of data Handling (GMDH)

Machine learning has two objectives, one is to classify data based on models which have been developed, the other purpose is to make predictions for future outcomes based on these models [64–67]. Artificial neural networks (ANNs) are a subset of machine learning and are at the heart of deep learning algorithms [68–75]. Group Method of Data Handling (GMDH) is an ANN model that is utilized for the purposes of

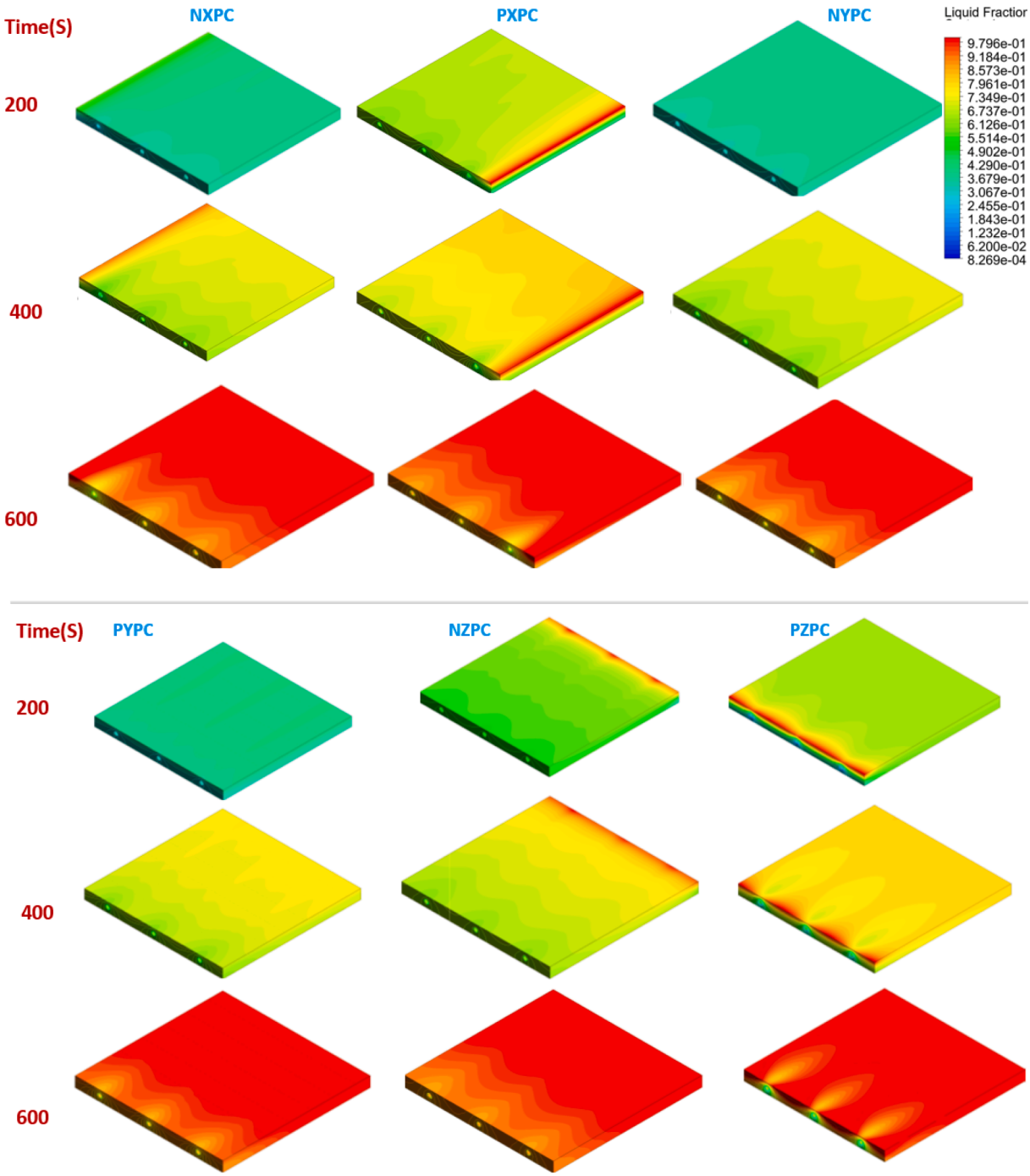

Fig. 9. Contour of melting fraction changes for different porous foam gradient states in C0.

data identification, prediction, and classification. GMDH is an advanced statistical training technology that has emerged from cybernetic research, specifically in the areas of self-organizing systems, control theory, information theory, and computer science. The primary objective of the GMDH network is to establish a function within a network utilizing the quadratic transfer function (TF). This process aims to address the statistical limitations of conventional neural networks. The selection of efficient input variables, determination of the number of layers and neurons, identification of hidden layers, and optimal model structure are all automatically decided by the GMDH system. GMDH is widely employed for modeling intricate systems and forecasting multivariate processes [58,59].

GMDH is widely used for modeling complex systems and predicting multivariate processes. The GMDH-NN has been created by using a network structure for the GMDH algorithm, and thus has had a significant impact on software implementation and understanding. The GMDH-NN contains a set of neurons that arise through one or more quadratic polynomials. In GMDH-NN, the most common neurons in each layer can only connect to the neurons of the previous layer. To specify GMDH-NN, it is necessary to remove the condition of using the adjacent layer to build the next layer. The self-organizing NN in the GMDH algorithm has contributed to the success of this algorithm in various scientific fields. This model has the structure of a multi-layered and progressive network. Every layer consists of one or more processing units (neurons), each of which has two inputs and one output. The TF is in the form of polynomials whose coefficients are obtained using

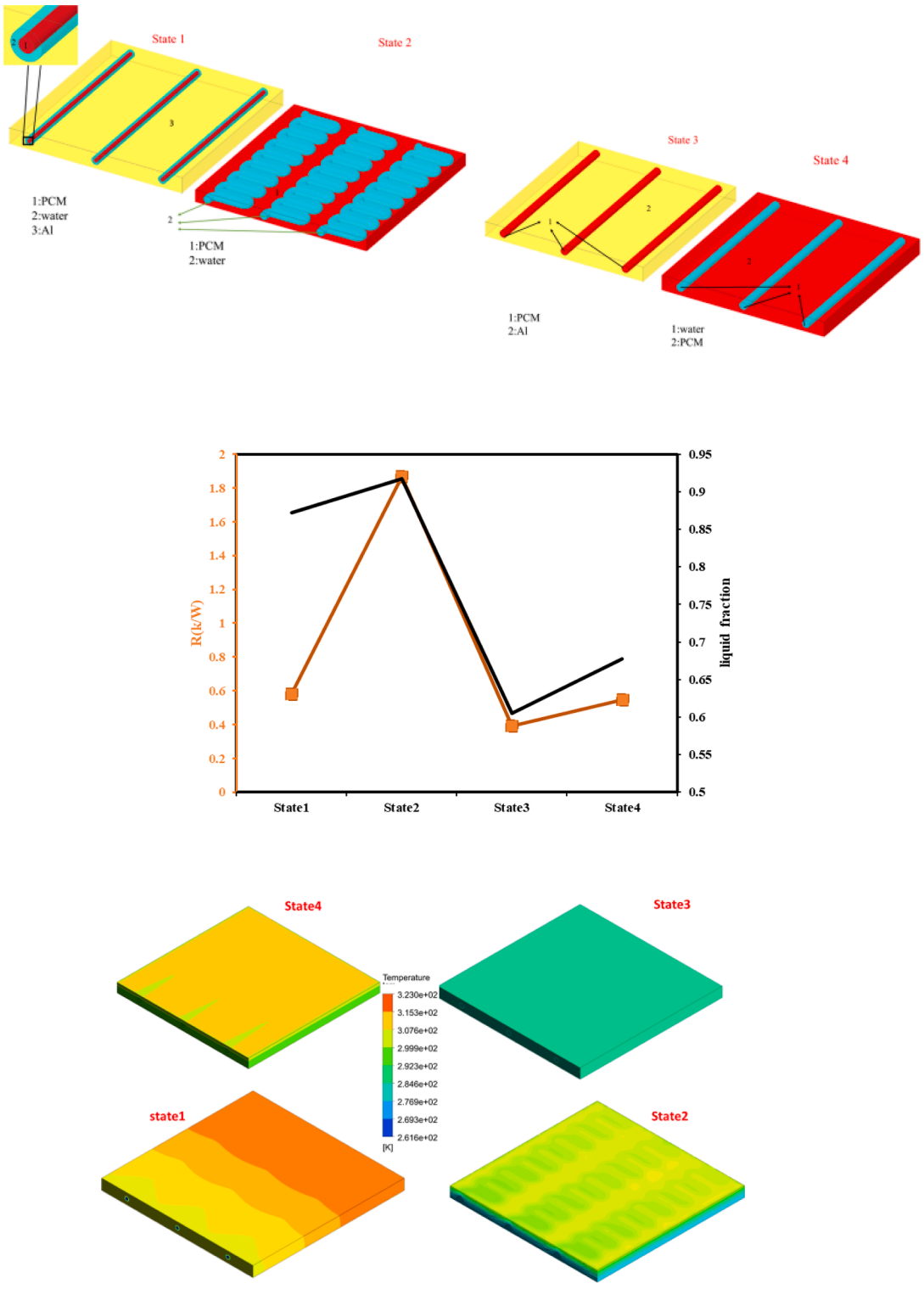

Fig. 10. Evaluation of PCM position on the TPEF of the MCHS and liquid fraction.

regression techniques [33]. Fig. 11 displays the structure of a general GMDH-NN using bivariate polynomial functions and the solution algorithm. In this simulation, the input variables are $k_{eff}\left(=\varepsilon k_f+(1-\varepsilon)k_s\right), \varphi, N, \mathrm{Pr}, \mathrm{Re}, \mathrm{Z}, \mathrm{Se}=\tau/\mathrm{C_p}(\theta_l-\theta_s)$ and *Da* and the output variable is *R*. Maximum number of neurons in a layer and maximum number of layers are 15& 4. Train ratio and test ratio are 0.85&0.15, respectively.

3.4.2. Multivariate polynomial regression (MPR)

By using multivariate polynomial regression [61–63], the prediction of *R* in terms of inputs has been discussed as follows:

$$\mathrm{R}=\mathrm{a}_0+\sum_{i=1}^{m} b_i X_i+\sum_{i=1}^{m}\sum_{j=1}^{m} C_{ij} X_i X_j \tag{5}$$

$X = k_{eff}, \varphi, N, \mathrm{Pr}, \mathrm{Re}, \mathrm{Z}, \mathrm{Se}$ and Da $\quad m = 8$

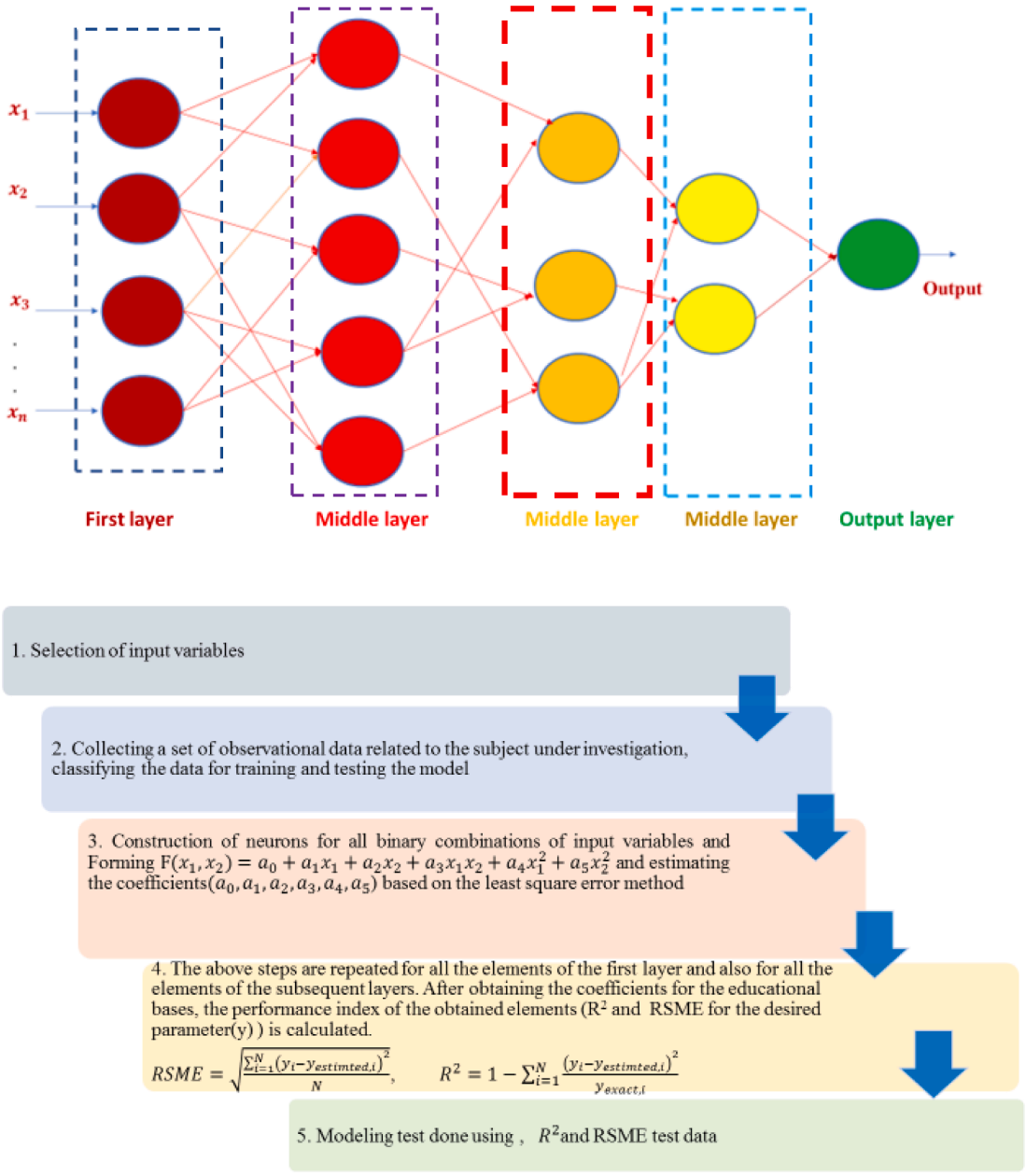

Fig. 11. GMDH network algorithm and structure [60].

The coefficients of the above equation are predicted by using the error square function and pattern search algorithm. The equation for R is estimated using the available data as follows as:

$$\begin{aligned} R = {} & 0.86ZSe + 82A02ReDa - 0.1058ReSe - 1.22ReZ - 41.6Pr - 73.61PrDa \\ & + 0.699PrSe + 0.1468PrRe + 0.0027NRe + 0.246NPr + 7860.0025\varphi Se \\ & - 40.72\varphi Re + 196.798\varphi Pr - 85.8\varphi N + 1.239k_{eff} - 75.823k_{eff}Da \\ & + 0.0159k_{eff}Se + 0.102k_{eff}Z - 0.00182k_{eff}Re \\ & - 0.175k_{eff}Pr - 0.025k_{eff}N + 2.744\varphi k_{eff} + 0.00021k_{eff}^2 + 2214.3137\varphi^2 \\ & + 0.441N^2 + 5.372\overset{2}{\mathrm{Pr}} + 0.00001Re^2 + 37.045Z^2 - 0.0004Se^2 + 0.636Da^2 \end{aligned} \quad (6)$$

The results of the estimation using both methods in the present study are shown in Fig. 12. R^2 values indicate the accuracy of the models: 0.996 for GMDH and 0.942 for MPR. These results demonstrate that the GMDH model outperforms the MPR model in accurately estimating the R.

4. Conclusion

Considering the sensitivity of electronic components to temperature increase, proper thermal design is required for this equipment to eliminate high heat flux. As systems are becoming smaller day by day, researchers from various fields have analyzed fluid flow in microchannels, which is of interest. Microchannels-Heat sink (MCHS) has been proposed as one of the latest cooling options for high-use electronic equipment due to its high convection heat transfer coefficient of fluid and the ability to reject high heat flux in a small volume. In this study, the effectiveness of using PCM, nano-PCM, and porous foam gradient on the thermal performance (TPEF) of MCHS has been investigated. The results of the study can be summarized as follows:

- Thermal resistance (R) decreases with increasing Re. The use of spiral microchannels reduces the amount of R and improves the TPEF. The addition of aluminum oxide and iron oxide nanoparticles to water improves the TPEF and reduces R. For Fe3O4-water and

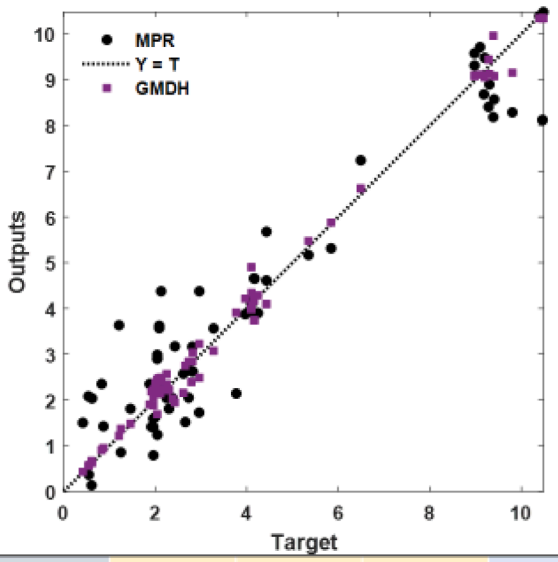

		GMDH		MPR
	Train data	Test data	All data	All data
RSME	0.228	0.227	0.238	0.9626
MSE	0.06	0.06	0.07	0.9266
R^2	0.99639	0.99788	0.99638	0.942

Fig. 12. Estimate R using both suggested models.

Al2O3-water, an increase in volume fraction from 0.01 to 0.05 results in a decrease of R by 8.6% and 4.3% for the flat tube(C0) and 8.3% and 5.1% for the spiral tube(C1), respectively.

- The use of PCM is effective on the thermal performance of MCHS. It is found that ENCAPSUL-PCM has the lowest R, while RT82-PCM has the highest R compared to the state without PCM. The combination of PCM-nanoparticles and hybrid nanoparticles has a significant impact on improving the TPEF. The type of nanoparticle can be effective on the TPEF according to its thermophysical properties. With an increase in Re from 50 to 800, there is about a 67% decrease in R by using Al2O3-Cu-PCM.
- The use of porous medium under the active surface can be effective in reducing R. Characteristics of porous medium: Darcy number, porosity coefficient (ε) and type of porous medium can affect the TPEF of MCHS. The best TPEF occurs in Darcy number = 0.001, ε = 0.9 and material: copper. Six porous foam gradient modes (by changing the porosity coefficient in the six main coordinate directions) have been considered. A porous foam gradient can affect the TPEF. The NYPC mode (ε enlarges linearly in the negative direction of the y-axis) has the best TPEF of MCHS.
- TPEF (or R) has been estimated using soft calculations: (Group Method of Data Handling (GMDH) and multivariate polynomial regression (MPR)). The GMDH model has provided a more accurate prediction.

Declaration of Competing Interest

The authors declare that they have no known competing financial interests or personal relationships that could have appeared to influence the work reported in this paper.

References

[1] P. Pontes, I. Gonçalves, M. Andredaki, A. Georgoulas, A. Moreira, A.S. Moita, Fluid flow and heat transfer in microchannel devices for cooling applications: Experimental and numerical approaches, Appl. Therm. Eng. 218 (2023), 119358.
[2] S.D. Farahani, A.D. Farahani, E. Hajian, Effect of PCM and porous media/nanofluid on the thermal efficiency of microchannel heat sinks, Int. Commun. Heat Mass Transfer 127 (2021), 105546.
[3] C. Xiao, M. Nourbakhsh, A. Alizadeh, D. Toghraie, P. Barnoon, A. Khan,, Investigation of thermal behavior and performance of different microchannels: A case study for traditional and Manifold Microchannels, Case Stud. Therm. Eng. 39 (2022), 102393.
[4] W.-M. Yan, C. Ho, Y.-T. Tseng, C. Qin, S. Rashidi, Numerical study on convective heat transfer of nanofluid in a minichannel heat sink with micro-encapsulated PCM-cooled ceiling, Int. J. Heat Mass Transf. 153 (2020), 119589.
[5] M.I. Hasan, D.M. Muter, Numerical investigation the performance of micro channel heat sink with different cooling mediums, Univ. Thi-Qar J. Eng. Sci. 10 (1) (2019) 101–113.
[6] M. Ahmadian-Elmi, M. Hajmohammadi, S. Nourazar, K. Vafai, M. Shafii, Effect of filling ratio, number of loops, and transverse distance on the performance of pulsating heat pipe in a microchannel heat sink, Numer. Heat Transfer, Part A: Appl. (2023) 1–22.
[7] M. Ahmadian-Elmi, M.R. Hajmohammadi, S.S. Nourazar, K. Vafai, M.B. Shafii, Investigating the effect of the presence of a pulsating heat pipe on the geometrical parameters of the microchannel heat sink, Numer. Heat Transfer, Part A: Appl. (2023) 1–17.
[8] A. Shahsavar, M.M. Baseri, A.A. Al-Rashed, M. Afrand, Numerical investigation of forced convection heat transfer and flow irreversibility in a novel heatsink with helical microchannels working with biologically synthesized water-silver nanofluid, Int. Commun. Heat Mass Transfer 108 (2019), 104324.
[9] O. Pourmehran, M. Rahimi-Gorji, M. Hatami, S. Sahebi, G. Domairry, Numerical optimization of microchannel heat sink (MCHS) performance cooled by KKL based nanofluids in saturated porous medium, J. Taiwan Inst. Chem. Eng. 55 (2015) 49–68.
[10] M. Hajmohammadi, M. Bahrami, M. Ahmadian-Elmi, Thermal performance improvement of microchannel heat sinks by utilizing variable cross-section microchannels filled with porous media, Int. Commun. Heat Mass Transfer 126 (2021), 105360.
[11] M. Hajmohammadi, S. Gholamrezaie, A. Ahmadpour, Z. Mansoori, Effects of applying uniform and non-uniform external magnetic fields on the optimal design of microchannel heat sinks, Int. J. Mech. Sci. 186 (2020), 105886.
[12] M. Ghorbani, M.R. Salimpour, K. Vafai, Microchannel thermal performance optimization utilizing porous layer configurations, Int. J. Heat Mass Transf. 133 (2019) 62–72.
[13] F. Li, Q. Ma, G. Xin, J. Zhang, X. Wang, Heat transfer and flow characteristics of microchannels with solid and porous ribs, Appl. Therm. Eng. 178 (2020), 115639.
[14] K. Al Khasawneh, I.A. Zahedah, M.O.A. Saileek, Gaseous slip flow in a porous two-dimensional rectangular microchannel subjected to inclined magnetic field, Results Eng. 16 (2022), 100720.
[15] Y.-M. Chu, U. Farooq, N.K. Mishra, Z. Ahmad, F. Zulfiqar, S. Yasmin, S.A. Khan, CFD analysis of hybrid nanofluid-based microchannel heat sink for electronic chips cooling: Applications in nano-energy thermal devices, Case Stud. Therm. Eng. 44 (2023), 102818.
[16] K. Tang, G. Lin, Y. Guo, J. Huang, H. Zhang, J. Miao, Simulation and optimization of thermal performance in diverging/converging manifold microchannel heat sink, Int. J. Heat Mass Transf. 200 (2023), 123495.
[17] X.-Y. Li, S.-L. Wang, X.-D. Wang, T.-H. Wang, Selected porous-ribs design for performance improvement in double-layered microchannel heat sinks, Int. J. Therm. Sci. 137 (2019) 616–626.
[18] S. Hassani, M. Khoshvaght-Aliabadi, S. Mazloumi, S. Rehman, A. Alimoradi, Improving thermal performance of microchannels by combining rectangular pin with chamber, Appl. Therm. Eng. 186 (2021), 116373.
[19] J.-F. Zhong, S.N. Sedeh, Y.-P. Lv, B. Arzani, D. Toghraie, Investigation of Ferro-nanofluid flow within a porous ribbed microchannel heat sink using single-phase and two-phase approaches in the presence of constant magnetic field, Powder Technol. 387 (2021) 251–260.
[20] M. Jamshidmofid, M. Bahiraei, Hydrothermal performance of single and hybrid nanofluids in Left-Right and Up-Down wavy microchannels using two-phase mixture approach, Int. Commun. Heat Mass Transfer 129 (2021), 105752.
[21] S. Sindhu, B. Gireesha, D. Ganji, Simulation of Cu: γ– ALOOH/Water in a microchannel heat sink by dint of porous media approach, Case Stud. Therm. Eng. 21 (2020), 100723.
[22] S. Bazkhane, I. Zahmatkesh, Taguchi–based sensitivity analysis of hydrodynamics and heat transfer of nanofluids in a microchannel heat sink (MCHS) having porous substrates, Int. Commun. Heat Mass Transfer 118 (2020), 104885.
[23] B. Rajabifar, Enhancement of the performance of a double layered microchannel heatsink using PCM slurry and nanofluid coolants, Int. J. Heat Mass Transf. 88 (2015) 627–635.
[24] P. Srivastava, R.I. Patel, A. Dewan, A study on thermal characteristics of double-layered microchannel heat sink: Effects of bifurcation and flow configuration, Int. J. Therm. Sci. 162 (2021), 106791.
[25] M. Hatami, D. Ganji, Thermal and flow analysis of microchannel heat sink (MCHS) cooled by Cu–water nanofluid using porous media approach and least square method, Energ. Conver. Manage. 78 (2014) 347–358.

[26] A. Maheswari, Y.K. Prajapati, Thermal performance enhancement and optimization of double-layer microchannel heat sink with intermediate perforated rectangular fins, Int. J. Therm. Sci. 185 (2023), 108043.
[27] P. Srivastava, R.I. Patel, A. Dewan, Thermal performance study of double-layer microchannel with bifurcation, Therm. Sci. Eng. Progress 17 (2020), 100481.
[28] D. Jing, L. He, Numerical studies on the hydraulic and thermal performances of microchannels with different cross-sectional shapes, Int. J. Heat Mass Transf. 143 (2019), 118604.
[29] R. Kothari, S.K. Sahu, S.I. Kundalwal, P. Mahalkar, Thermal performance of phase change material–based heat sink for passive cooling of electronic components: An experimental study, Int. J. Energy Res. 45 (4) (2021) 5939–5963.
[30] R. Kothari, S.K. Sahu, S.I. Kundalwal, S. Sahoo, Experimental investigation of the effect of inclination angle on the performance of phase change material based finned heat sink, J. Storage Mater. 37 (2021), 102462.
[31] A. Kumar, R. Kothari, S.K. Sahu, S.I. Kundalwal, A comparative study and optimization of phase change material based heat sinks for thermal management of electronic components, J. Storage Mater. 43 (2021), 103224.
[32] C. Ho, S.-T. Hsu, S. Rashidi, W.-M. Yan, Water-based nano-PCM emulsion flow and heat transfer in divergent mini-channel heat sink—an experimental investigation, Int. J. Heat Mass Transf. 148 (2020), 119086.
[33] L. Dong, Y. Li, J. Li, Y. Guan, X. Chen, D. Zhang, Z. Wang, Mesoporous carbon hollow spheres encapsulated phase change material for efficient emulsification of high-viscosity oil, J. Hazard. Mater. 451 (2023), 131112.
[34] S.D. Farahani, A.D. Farahani, E. Hajian, H.F. Öztop, Control of PCM melting process in an annular space via continuous or discontinuous fin and non-uniform magnetic field, J. Storage Mater. 55 (2022), 105410.
[35] S.D. Farahani, A.D. Farahani, P. Oraki, Improving thermal performance of solar water heater using phase change material and porous material, Heat Transfer Res. 52 (16) (2021).
[36] S.D. Farahani, A.D. Farahani, F. Tayebzadeh, H.F. Öztop, The effect of novel fin shapes and non-uniform magnetic field on the nanoparticles embedded PCM melting in a tube, J. Magn. Magn. Mater. 562 (2022), 169826.
[37] A. Chibani, S. Merouani, H. Laidoudi, A. Dehane, M.R. Morakchi, L. Bendada, Analysis and optimization of concentrator photovoltaic system using a phase change material (RT 35HC) combined with variable metal fins, J. Storage Mater. 72 (2023), 108283.
[38] A. Chibani, A. Dehane, S. Merouani, The sono-PCM reactors: A new approach for recovering the heat dissipated from ultrasonic reactors using a phase change material, Int. J. Heat Mass Transf. 215 (2023), 124505.
[39] A. Chibani, A. Dehane, S. Merouani, O. Hamdaoui, Phase. Change. Material (PCM)-based thermal. storage system for managing the sonochemical reactor heat: Thermodynamic analysis of the liquid height impact, Ultrasonics Sonochemistry, (2023) 106483.
[40] A. Chibani, S. Merouani, F. Benmoussa, M.H. Abdellattif, A. Erto, B.-H. Jeon, Y. Benguerba, A strategy for enhancing heat transfer in phase change material-based latent thermal energy storage unit via nano-oxides addition: A study applied to a shell-and-tube heat exchanger, J. Environ. Chem. Eng. 9 (6) (2021), 106744.
[41] K.N. Ramesh, T.K. Sharma, G.A.P. Rao, K.M. Murthy, Numerical Investigation on Thermal Performance of PCM-Based Hybrid Microchannel Heat Sinks for Electronics Cooling Application, Arab. J. Sci. Eng. (2022) 1–15.
[42] H. Dai, W. Chen, X. Dong, Y. Liu, Q. Cheng, Thermohydraulic performance analysis of graded porous media microchannel with microencapsulated phase change material suspension, Int. J. Heat Mass Transf. 176 (2021), 121459.
[43] H. Dai, W. Chen, Q. Cheng, Y. Liu, X. Dong, Analysis of thermo-hydraulic characteristics in the porous-wall microchannel with microencapsulated phase change slurry, Int. J. Heat Mass Transf. 165 (2021), 120634.
[44] P. Wang, M. Li, B. Dai, Q. Wang, Y. Ma, C. Dang, H. Tian, Experimental and analytical investigation of CO2/R32 condensation heat transfer in a microchannel, Int. J. Refrig 145 (2023) 338–352.
[45] M. Vajdi, F.S. Moghanlou, E.R. Niari, M.S. Asl, M. Shokouhimehr, Heat transfer and pressure drop in a ZrB2 microchannel heat sink: a numerical approach, Ceram. Int. 46 (2) (2020) 1730–1735.
[46] S.D. Farahani, A.D. Farahani, H.F. Öztop, Scrutiny of melting rate of phase change material in a four petals cavity with internal Branch fins under magnetic field, J. Magn. Magn. Mater. 170727 (2023).
[47] S.D. Farahani, A.D. Farahani, A.J. Mamoei, W.-M. Yan, Enhancement of phase change material melting using nanoparticles and magnetic field in the thermal energy storage system with strip fins, J. Storage Mater. 57 (2023), 106282.
[48] A. Joseph, S. Sreekumar, C.S. Kumar, S. Thomas, Optimisation of thermo-optical properties of SiO2/Ag–CuO nanofluid for direct absorption solar collectors, J. Mol. Liq. 296 (2019), 111986.
[49] M. Ghanbarpour, E.B. Haghigi, R. Khodabandeh, Thermal properties and rheological behavior of water based Al2O3 nanofluid as a heat transfer fluid, Exp. Therm Fluid Sci. 53 (2014) 227–235.
[50] A. Mishra, H. Upreti, A comparative study of Ag–MgO/water and Fe3O4–CoFe2O4/EG–water hybrid nanofluid flow over a curved surface with chemical reaction using Buongiorno model, Partial Differential Equations in Applied Mathematics 5 (2022), 100322.
[51] C. Li, M. Li, Y. Li, Tailored calcium chloride hexahydrate as a composite phase change material for cold storage, J. Storage Mater. 56 (2022), 105798.
[52] L. Socaciu, A. Pleșa, P. Ungureșan, O. Giurgiu, Review on phase change materials for building applications, Leonardo Electronic J. Practices Technol. 25 (2014) 179–194.
[53] K. Nagano, T. Mochida, S. Takeda, R. Domański, M. Rebow, Thermal characteristics of manganese (II) nitrate hexahydrate as a phase change material for cooling systems, Appl. Therm. Eng. 23 (2) (2003) 229–241.
[54] M.F. Junaid, Z. ur Rehman, M. Čekon, J. Čurpek, R. Farooq, H. Cui, I. Khan, Inorganic phase change materials in thermal energy storage: A review on perspectives and technological advances in building applications, Energy Build. 252 (2021) 111443.
[55] F. Hassan, F. Jamil, A. Hussain, H.M. Ali, M.M. Janjua, S. Khushnood, M. Farhan, K. Altaf, Z. Said, C. Li, Recent advancements in latent heat phase change materials and their applications for thermal energy storage and buildings: A state of the art review, Sustain. Energy Technol. Assess. 49 (2022), 101646.
[56] R. Yamada, T. Taguchi, N. Igawa, Mechanical and thermal properties of 2D and 3D SiC/SiC composites, J. Nucl. Mater. 283 (2000) 574–578.
[57] R.J. Phillips, Microchannel heat sinks, The Lincoln Laboratory Journal 1 (1) (1988) 31–48.
[58] A. Ivakhnenko, G. Ivakhnenko, The review of problems solvable by algorithms of the group method of data handling (GMDH), Pattern recognition and image analysis c/c of raspoznavaniye obrazov i analiz izobrazhenii 5 (1995) 527–535.
[59] L. Anastasakis, N. Mort, The development of self-organization techniques in modelling: a review of the group method of data handling (GMDH), Research Report-University of Sheffield Department of Automatic Control and Systems Engineering, (2001).
[60] S.J. Farlow, The GMDH algorithm of Ivakhnenko, Am. Stat. 35 (4) (1981) 210–215.
[61] H. Imran, N.M. Al-Abdaly, M.H. Shamsa, A. Shatnawi, M. Ibrahim, K.A. Ostrowski, Development of prediction model to predict the compressive strength of eco-friendly concrete using multivariate polynomial regression combined with stepwise method, Materials 15 (1) (2022) 317.
[62] S. Kim, S. Kim, C.H. Green, J. Jeong, Multivariate polynomial regression modeling of total dissolved-solids in rangeland stormwater runoff in the Colorado River Basin, Environ. Model. Softw. 157 (2022), 105523.
[63] V. Narayan, A. Daniel, Energy Efficient Protocol for Lifetime Prediction of Wireless Sensor Network using Multivariate Polynomial Regression Model, J. Sci. Ind. Res. 81 (12) (2022) 1297–1309.
[64] C. Hebbi, H.R. Mamatha, Comprehensive dataset building and recognition of isolated handwritten kannada characters using machine learning models, Artificial Intelligence and Applicatons (2023), https://doi.org/10.47852/bonviewAIA3202624.
[65] Y. Guo, Z. Mustafaoglu, D. Koundal, Spam Detection Using Bidirectional Transformers and Machine Learning Classifier Algorithms, Journal of Computational and Cognitive Engineering (2022), https://doi.org/10.47852/bonviewJCCE220219.
[66] H. Gaur, B. Khidhir, R.K. Manchiryal, Solution of structural mechanic's problems by machine learning, Int. J. Hydromechatronics 5 (1) (2022) 22–43.
[67] B.K. Liu, W.Z. Lu, Surrogate models in machine learning for computational stochastic multi-scale modelling in composite materials design, Int. J. Hydromechatronics 5 (4) (2022) 336–365.
[68] N. Luo, et al., Fuzzy logic and neural network-based risk assessment model for import and export enterprises: A review, Journal of Data Science and Intelligent Systems (2023), https://doi.org/10.47852/bonviewJDSIS32021078.
[69] B. Peng, et al., 3D-STCNN: Spatiotemporal Convolutional Neural Network based on EEG 3D features for detecting driving fatigue, Journal of Data Science and Intelligent Systems (2023), https://doi.org/10.47852/bonviewJDSIS3202983.
[70] Z. Li, S. Li, Recursive recurrent neural network: a novel model for manipulator control with different levels of physical constraints, CAAI Trans. Intell. Technol. (2022) 1–13, https://doi.org/10.1049/cit2.12125.
[71] Q. Zhang, et al., A robust deformed convolutional neural network (CNN) for image denoising, CAAI Trans. Intell. Technol. (2022) 1–12, https://doi.org/10.1049/cit2.12110.
[72] P. Preethi, H.R. Mamatha, Region-based convolutional neural network for segmenting text in epigraphical images, Artificial Intelligence and 1 (2) (2023) 119–127, https://doi.org/10.47852/bonviewAIA2202293.
[73] Z. Chen, Research on Internet Security Situation Awareness Prediction Technology based on Improved RBF Neural Network Algorithm, Journal of Computational and Cognitive Engineering (2022), https://doi.org/10.47852/bonviewJCCE149145205514.
[74] A. Alizadeh, K. Jasim Mohammed, G. Fadhil Smaisim, S.K. Hadrawi, H. Zekri, H. Taheri Andani, N. Nasajpour-Esfahani, D. Toghraie, Evaluation of the effects of the presence of ZnO -TiO2 (50 %–50 %) on the thermal conductivity of Ethylene Glycol base fluid and its estimation using Artificial Neural Network for industrial and commercial applications, Journal of Saudi Chemical Society 27 (2) (2023) 101613, https://doi.org/10.1016/j.jscs.2023.101613.
[75] X. Dai, H.T. Andani, A. Alizadeh, A.M. Abed, G.F. Smaisim, S.K. Hadrawi, M. Karimi, M. Shamsborhan, D. Toghraie, Using Gaussian Process Regression (GPR) models with the Matérn covariance function to predict the dynamic viscosity and torque of SiO2/Ethylene glycol nanofluid: A machine learning approach, Engineering Applications of Artificial Intelligence 122 (106107) (2023) 106107, https://doi.org/10.1016/j.engappai.2023.106107.